

Peridynamics-based discrete element method (PeriDEM) model of granular systems involving breakage of arbitrarily shaped particles

Prashant K. Jha^{a,1,*}, Prathamesh S. Desai^{b,2}, Debdeep Bhattacharya^{c,3}, Robert Lipton^{c,4}

^a*Oden Institute for Computational Engineering and Sciences, The University of Texas at Austin, TX*

^b*Department of Mechanical Engineering, Rice University, Houston, TX*

^c*Department of Mathematics, Louisiana State University, Baton Rouge, LA*

Abstract

Usage, manipulation, transport, delivery, and mixing of granular or particulate media, comprised of spherical or polyhedral particles, is commonly encountered in industrial sectors of construction (cement and rock fragments), pharmaceutics (tablets), and transportation (ballast). Elucidating the behavior of particulate media, in concert with particle attrition (i.e., particle wear and subsequent particle fragmentation) is essential for predicting the performance and increasing the efficiency of engineering systems using such media. Discrete element method (DEM) based techniques can describe the interaction between particles but cannot model intra-particle deformation, especially intra-particle fracture. On the other hand, peridynamics provides the means to account for intra-particle deformation and fracture due to contact forces between particles. The present study proposes a hybrid model referred to as *PeriDEM* that combines the advantages of peridynamics and DEM. The model parameters can be tuned to achieve desired DEM contact forces, damping effects, and intra-particle stiffness. Two particle impacts and compressive behavior of multi-particle systems are thoroughly investigated. The effect of mesh resolution on intra-particle peridynamics is explicitly studied. The proposed hybrid PeriDEM model opens a new avenue to explore the complicated interactions encountered in discrete particle dynamics that involve formation of force chains, particle interlocking, particle attrition, and the eventual breakage.

Keywords: Peridynamics, discrete element method, particle attrition, particle interlocking, particle breakage, granular media, fracture

1. Introduction

Granular media consists of a collection of mesoscale to macro-scale solid particles. Modeling granular media is a challenging problem as it involves the correct modeling of contact forces between particles with an arbitrary boundary and deformation within each particle including fracture/plasticity/corrosion. Additional issues beyond contact forces and inter-particle fracture or

*Corresponding author (pjha@utexas.edu)

Email addresses: pjha@utexas.edu (Prashant K. Jha), pdesai@rice.edu (Prathamesh S. Desai), debdeepbh@lsu.edu (Debdeep Bhattacharya), lipton@lsu.edu (Robert Lipton)

¹Website: <https://prashjha.github.io/>

²Website: <https://sites.google.com/site/pratnsaiweb/>

³Website: <https://debdeepbh.github.io/>

⁴Website: <https://www.math.lsu.edu/~lipton/index.html>

damage need to be considered, such as the effect of entrained gas/fluid on granular media dynamics. The discrete element method (DEM for short), introduced in Cundall and Strack [1], provides a framework in which linear and angular displacements and velocities of individual particles are solved using Newton's second law. The contact forces, moments, friction forces, and damping forces between two particles in direct contact are postulated to assume that the particles are spherical (disks in 2D). Particles in DEM are assumed to retain their shape, allowing one to only focus on contact related interactions. DEM has been applied to problems involving powder dynamics in additive manufacturing and rock mechanics Desai [2], particle packing, mixing and segregation Labra and Onate [3], Yan et al. [4], particle transport and particle-fluid interaction Feng et al. [5], Zhu et al. [6], among other applications. DEM based methods have been extended to handle the arbitrary shaped particles and particle breakage using cohesive interactions Neveu et al. [7], Nguyen et al. [8].

Under high loading, the particle's internal deformation becomes a major factor in particulate media dynamics. Particles may undergo a change in shape, and they may yield or eventually break. Intra-particle deformation requires modeling each particle as a discrete continuum solid with appropriate constitutive law, e.g., linear/nonlinear elasticity, LEFM, plasticity, etc. As the particle deforms, it changes its shape and can break into smaller particles; hence the contact forces with adjacent particles become difficult to model. In this study, we consider peridynamics model for the internal particle deformation and/or fracture. In peridynamics, the internal forces at a material point are expressed using a summation of pairwise forces with material points inside a neighborhood of interaction. This is in contrast with the classical continuum mechanics in which the divergence of stress gives the force at a material point. This was originally proposed in Silling [9]. Since then, the theory has gained a good deal of attention Silling et al. [10], Foster et al. [11], Bobaru and Hu [12], Lipton [13], Lipton et al. [14], Jha and Lipton [15]. Because of its ability to handle the fracture process, the theory has seen great success in modeling fracture in solids Silling and Askari [16], Silling and Bobaru [17], Ha and Bobaru [18], Diehl et al. [19], Behzadinasab et al. [20], Lipton et al. [21], Jha and Lipton [15], Wu et al. [22], modeling corrosion Chen and Bobaru [23], Jafarzadeh et al. [24], erosion Zhang et al. [25], and porous flow using peridynamics Katiyar et al. [26], Ouchi et al. [27]. In peridynamics, both an elastic deformation and crack emerge from the dynamics, and no additional rule or hypothesis is required to govern the crack tip motion Silling [9]. Recently it is shown that the Linear Elastic Fracture Mechanics (LEFM) kinetic relation for crack tip velocity is recovered from the peridynamics equation of motion as the length scale of non-locality approaches zero Lipton and Jha [28], Jha and Lipton [15].

In this work, we combine the Peridynamics theory with DEM to expand the scope of DEM to a large class of problems where particle deformation and breakage can cause significant changes in particle dynamics. The earlier work Behzadinasab et al. [20] applied peridynamics to model both inter-particle and intra-particle interactions. Recently Zhu and Zhao [29] proposed a model that utilizes peridynamics for intra-particle deformation and non-smooth contact dynamics for particle-particle interaction. The present work takes the idea in Behzadinasab et al. [20] forward by carefully incorporating the three major components of the contact in DEM based methods: normal contact force, frictional force, and damping force to model inter-particle interaction while using peridynamics to model intra-particle interactions. Deformation within each particle in the media is governed by the peridynamics. Particle mechanically interacts with the surrounding particles and through DEM like contact laws, applied between the material points of two particles in contact, particles exchange force. Contact laws are defined on the discretization of the particle. A pair of

nodes (discrete points in a meshless discretization) from two distinct particles, if sufficiently close, can exert contact forces on each other. The interaction between nodes of two particles in contact is based on the general spring-dashpot system where the force due to spring is a normal contact force and the force due to dashpot is a dissipative damping force.

In addition to this, we also add the component to the spring-dashpot that gives the frictional force between two sufficiently close nodes. The spring-dashpot system parameters can be calibrated to achieve the desired damping effect and the desired stiffness between the particles. Such a treatment is similar to DEM based methods where the virtual simulator of a granular media is first calibrated Desai et al. [30], Asmar et al. [31] using the experimental data. In this paper, we apply our model to a ladder of problems of increasing complexity. First, we show the damping effect on two-particle collision and demonstrate that the damping parameter can be tuned for the desired damping effect. We consider the effect of mesh size on the two-particle system. Since the contact laws are directly applied in the discretization, some effect of mesh size is to be expected. The results show that mesh effects are within a reasonable range and can be adequately understood. Finally, we apply the model to a compressive test consisting of a collection of particles confined to a rectangular domain with the top wall of the domain moving into the suspension at a prescribed speed. While the method shows promising results for the breakage of particulate media, it is computationally costly. The computational expense can be attributed to the nonlocal force calculations in each particle and nonlocal search for nodes within two particles that are expected to collide. The model proposed here is a high fidelity model and can describe the interactions and internal deformation of a particle in a medium more accurately, and therefore the additional computational cost is justified. However, there are ways to significantly reduce the computational cost, such as treating particles as rigid bodies under small deformations and loading and otherwise treating them as a deformable solid. Future work will be towards the development of methods that reduce simulation cost enabling larger-scale simulations.

The paper is organized as follows: In [section 2](#), we present peridynamics for intra-particle interaction and DEM-like model for inter-particle interaction. We refer to the hybrid method as *PeriDEM*. In [section 3](#) we apply the model to various settings. We first analyze the damping effects under the simple two-particle system in [subsection 3.2](#). Next, we study the effects of mesh size on the inter-particle contact in [subsubsection 3.2.1](#). Having tested the model for a two-particle setting, we apply the model to study the compressive behavior of a multi-particle system [subsection 3.4](#). In [section 4](#), we present the discussion of the current work and future directions.

2. Development of the PeriDEM model

Let $\Omega \in \mathbb{R}^d$ denote the particulate media domain where $d = 2$ or 3 is the dimension. The media Ω consists of particles Ω_{p_i} , $i = 1, 2, \dots, N$, and is subjected to external forces or displacements altering the configuration of particles within it. There are two different interactions in the media: intra-particle interaction in which each particle reacts to surrounding boundary conditions and results in internal forces in each particle; and the inter-particle interaction in which pairs of particles come in contact and exchange forces at the interface. For the former, we consider the peridynamics description of solid deformation. For the latter, we propose a DEM-like model to account for the exchange of forces. Since the normal contact in the model is defined at the level of material points in the neighborhood of the contact region, the model can be used to describe the contact for arbitrarily shaped particles.

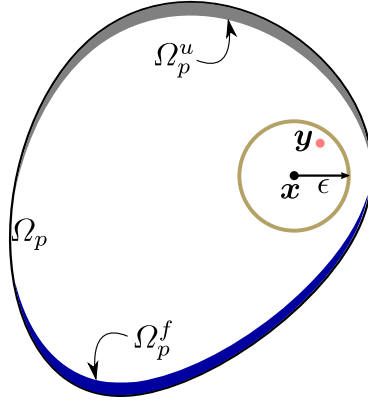


Figure 1: Typical particle domain. Here the internal force at \mathbf{x} is due to the interaction of \mathbf{x} with all the points $\mathbf{y} \in B_\epsilon(\mathbf{x})$. Displacement and force boundary conditions are specified in Ω_p^u and Ω_p^f respectively.

2.1. Intra-particle interaction: Peridynamics

Consider a typical particle in the media Ω_p . Let $\mathbf{x} \in \Omega_p$ denote the coordinate of material point and let $\mathbf{u} : \Omega_p \times [0, T] \rightarrow \mathbb{R}^d$ and $\mathbf{v} : \Omega_p \times [0, T] \rightarrow \mathbb{R}^d$ denote the displacement and velocity field. At any time $t \in [0, T]$, the new coordinate of material point $\mathbf{x} \in \Omega_p$ is given by $\mathbf{z}(\mathbf{x}, t) = \mathbf{x} + \mathbf{u}(\mathbf{x}, t)$. In peridynamics, the force at a material point is a result of pairwise forces acting on the point due to neighboring points. In a general form, the force at point $\mathbf{x} \in \Omega_p$ is given by

$$\mathbf{F}(\mathbf{x}, t; \mathbf{u}) = \int_{B_\epsilon(\mathbf{x}) \cap \Omega_p} \mathbf{f}(\mathbf{y}, \mathbf{x}) d\mathbf{y}, \quad (1)$$

where $B_\epsilon(\mathbf{x})$ is the ball of radius ϵ centered at \mathbf{x} , $\mathbf{f}(\mathbf{y}, \mathbf{x})$ is the pairwise force acting on material point \mathbf{x} due to interaction of \mathbf{x} with \mathbf{y} . $\epsilon > 0$ is the nonlocal length-scale which measures the extent of nonlocal interaction in the material. The motion of points in Ω_p is given by the Newton's second law of motion:

$$\rho \ddot{\mathbf{u}}(\mathbf{x}, t) = \mathbf{F}(\mathbf{x}, t; \mathbf{u}) + \mathbf{F}_{ext}(\mathbf{x}, t), \quad \forall (\mathbf{x}, t) \in \Omega_p \times [0, T], \quad (2)$$

where \mathbf{F}_{ext} is the external force such as contact force acting on \mathbf{x} . We close above system by specifying the initial condition

$$\mathbf{u}(\mathbf{x}, 0) = \mathbf{u}_0(\mathbf{x}), \quad \mathbf{v}(\mathbf{x}, 0) = \mathbf{v}_0(\mathbf{x}), \quad \forall \mathbf{x} \in \Omega_p \quad (3)$$

and boundary condition

$$\mathbf{u}(\mathbf{x}, t) = \mathbf{g}(\mathbf{x}), \quad \forall (\mathbf{x}, t) \in \Omega_p^u \times [0, T], \quad (4)$$

where \mathbf{g} is the specified displacement field, Ω_p^u is the part of Ω_p over which the displacement is specified, see Figure 1. Under suitable assumptions on \mathbf{f} , body forces and initial conditions it can be shown that the non local dynamics Equation 2 converges to the classical continuum mechanics equations $\rho \ddot{\mathbf{u}}(\mathbf{x}, t) = \nabla \cdot \boldsymbol{\sigma}$, inside the particle where $\boldsymbol{\sigma}$ is the Cauchy's stress away from the crack and the non-local dynamics delivers the classic equation of crack tip motion $G_c = \mathcal{J}$ where \mathcal{J} is the elastic energy flowing into the tip; see Lipton [13], Jha and Lipton [32, 15]. In the next section we show the specific form of force \mathbf{f} used here.

2.1.1. State-based peridynamics model

Within the peridynamics formulation there are two classes of models: bond-based and state-based. In bond-based models, the force between pair of material points only depends on displacement of the points. In contrast, in the state-based models, the force also depends on the volumetric deformation at pair of points. In this work, we consider state-based model Silling et al. [33]. Existing literature Silling et al. [33], Warren et al. [34] use the concept of states to describe the model. For simplicity, we present the model using the familiar notion of functions. The force acting on \mathbf{x} due to \mathbf{y} has following form Silling et al. [33]

$$\mathbf{f}(\mathbf{y}, \mathbf{x}) = \mathbf{T}_x(\mathbf{y}) - \mathbf{T}_y(\mathbf{x}), \quad (5)$$

and therefore total force density at material point \mathbf{x} is

$$\mathbf{F}(\mathbf{x}, t; \mathbf{u}) = \int_{B_\epsilon(\mathbf{x}) \cap \Omega_p} (\mathbf{T}_x(\mathbf{y}) - \mathbf{T}_y(\mathbf{x})) d\mathbf{y}. \quad (6)$$

Function $\mathbf{T}_x : B_\epsilon(\mathbf{x}) \rightarrow \mathbb{R}^d$ defined for each material point \mathbf{x} is given by

$$\mathbf{T}_x(\mathbf{y}) = \left[\kappa \frac{3J(|\mathbf{y} - \mathbf{x}|/\epsilon)|\mathbf{y} - \mathbf{x}| \theta_x}{m_x} + G \frac{15J(|\mathbf{y} - \mathbf{x}|/\epsilon)e_x^d(\mathbf{y})}{m_x} \right] \frac{\mathbf{z}(\mathbf{y}) - \mathbf{z}(\mathbf{x})}{|\mathbf{z}(\mathbf{y}) - \mathbf{z}(\mathbf{x})|}, \quad (7)$$

where $J(r) = 1 - r$ is the influence function, κ, G are bulk and shear modulus, m_x is a weighted volume of a material point, θ_x a dilation of material point, and $e_x^d(\mathbf{y})$ is the deviatoric part of the extension defined for \mathbf{y} in the neighborhood of a material point \mathbf{x} . $m_x, \theta_x, e_x^d(\mathbf{y})$ are given by

$$\begin{aligned} m_x &= \int_{B_\epsilon(\mathbf{x})} |\mathbf{y} - \mathbf{x}|^2 J(|\mathbf{y} - \mathbf{x}|/\epsilon) d\mathbf{y}, \\ \theta_x &= \frac{3}{m_x} \int_{B_\epsilon(\mathbf{x})} |\mathbf{y} - \mathbf{x}| (|\mathbf{z}(\mathbf{y}) - \mathbf{z}(\mathbf{x})| - |\mathbf{y} - \mathbf{x}|) J(|\mathbf{y} - \mathbf{x}|/\epsilon) d\mathbf{y}, \\ e_x^d(\mathbf{y}) &= |\mathbf{z}(\mathbf{y}) - \mathbf{z}(\mathbf{x})| - |\mathbf{y} - \mathbf{x}| - \frac{|\mathbf{y} - \mathbf{x}| \theta_x}{3}. \end{aligned} \quad (8)$$

We can write $\mathbf{T}_x(\mathbf{y})$ as follows

$$\mathbf{T}_x(\mathbf{y}) = J(|\mathbf{y} - \mathbf{x}|) |\mathbf{y} - \mathbf{x}| \theta_x \left(\frac{9\kappa}{m_x} - \frac{15G}{3m_x} \right) + J(|\mathbf{y} - \mathbf{x}|) (|\mathbf{z}(\mathbf{y}) - \mathbf{z}(\mathbf{x})| - |\mathbf{y} - \mathbf{x}|) \left(\frac{15G}{m_x} \right). \quad (9)$$

Modeling fracture. In peridynamics, the fracture is incorporated at the bond-level in which the bond between two material points can break if the bond is stretched beyond a critical stretch, Silling [9]. The crack/fracture is a results of collection of broken bonds. Given critical energy release rate, the critical stretch s_0 beyond which bond is broken is given by Zhu and Zhao [35],

$$s_0 = \sqrt{\frac{G_c}{(3\mu + (3/4)^4[\kappa - (5\mu/3)])\epsilon}}. \quad (10)$$

Let $h : \mathbb{R} \rightarrow [0, 1]$ be the function such that

$$h(s) = \begin{cases} 1 & \text{if } s < s_0, \\ 0 & \text{otherwise.} \end{cases} \quad (11)$$

Following the implementation in Peridigm library Littlewood et al. [36] we modify the $\mathbf{T}_x(\mathbf{y})$, to take into account the bond-breakage, as follows:

$$\begin{aligned} \mathbf{T}_x(\mathbf{y}) = h(s(\mathbf{y}, \mathbf{x}), t) & \left[J(|\mathbf{y} - \mathbf{x}|) |\mathbf{y} - \mathbf{x}| \theta_x \left(\frac{3\kappa}{m_x} - \frac{15G}{3m_x} \right) \right. \\ & \left. + J(|\mathbf{y} - \mathbf{x}|) (|\mathbf{z}(\mathbf{y}) - \mathbf{z}(\mathbf{x})| - |\mathbf{y} - \mathbf{x}|) \left(\frac{15G}{m_x} \right) \right] \frac{\mathbf{z}(\mathbf{y}) - \mathbf{z}(\mathbf{x})}{|\mathbf{z}(\mathbf{y}) - \mathbf{z}(\mathbf{x})|}, \end{aligned} \quad (12)$$

where θ_x is also modified to account for damage in bonds as follows:

$$\theta_x = \frac{3}{m_x} \int_{B_\epsilon(\mathbf{x})} h(s(\mathbf{y}, \mathbf{x}), t) |\mathbf{y} - \mathbf{x}| (|\mathbf{z}(\mathbf{y}) - \mathbf{z}(\mathbf{x})| - |\mathbf{y} - \mathbf{x}|) J(|\mathbf{y} - \mathbf{x}|/\epsilon) d\mathbf{y}. \quad (13)$$

Damage at material points. Consider a material point $\mathbf{x} \in \Omega_p$. The damage at point \mathbf{x} is defined as

$$Z(\mathbf{x}) = \sup_{\mathbf{y} \in B_\epsilon(\mathbf{x}) \cap \Omega_p} \frac{|\mathbf{u}(\mathbf{y}) - \mathbf{u}(\mathbf{x})|}{|\mathbf{y} - \mathbf{x}|} \frac{1}{s_0}, \quad (14)$$

where s_0 is the critical bond-strain. $Z(\mathbf{x}) < 1$ implies that deformation at the point \mathbf{x} is elastic and there are no broken bonds in the neighborhood of \mathbf{x} . In contrast, $Z(\mathbf{x}) \geq 1$ implies there are points in the neighborhood of \mathbf{x} such that bonds with those points are broken. The fracture zone is the region in Ω_p consisting of points with one or more broken bonds in the neighborhood, ie

$$FZ = \{\mathbf{x} \in \Omega_p : Z(\mathbf{x}) \geq 1\}. \quad (15)$$

2.2. Inter-particle interaction: DEM-like model

Let $\{\mathbf{x}_i, V_i\}_{i=1}^n$ represent the mesh describing particle Ω_p where \mathbf{x}_i is the coordinate of i^{th} node and V_i is the volume represented by that node. Suppose $\Omega_p, \Omega_{p'}$ are two particles in contact. Traditional DEM based methods apply contact force at the centroid of particles. In this work, we follow the alternative approach initially proposed in Behzadinasab et al. [20]. Here the idea is to apply the contact forces on discretization nodes of the two particles when they get sufficiently close. We propose a model that includes the principal contact forces, including the normal contact force, damping force, and friction force. The parameters in this model can be tuned to get the desired damping effect and desired contact strength. We assume that the points in the neighborhood of the contact surface of each particle are connected to their counterparts on the other particle by a generalized spring system that includes compressive force, damping force, and friction force, schematically shown in Figure 2. Since the contact forces are defined on the pair of discretization nodes, the model is not limited to spherical (convex) particles and can be applied to model the contact between particles of any arbitrary shapes.

Let $\mathbf{x} \in \Omega_p, \mathbf{x}' \in \Omega_{p'}$ are discretized nodes of particles $\Omega_p, \Omega_{p'}$. Let V, V' denote the volume represented by the nodes \mathbf{x}, \mathbf{x}' . We denote the current position of \mathbf{x}, \mathbf{x}' by \mathbf{z}, \mathbf{z}' . The nodes \mathbf{x}, \mathbf{x}' interact only when $|\mathbf{z} - \mathbf{z}'| < R_c$, where R_c is the radius of contact. Contact radius is typically chosen as $0.95h$ where h is the mesh size. We describe the contact forces next.

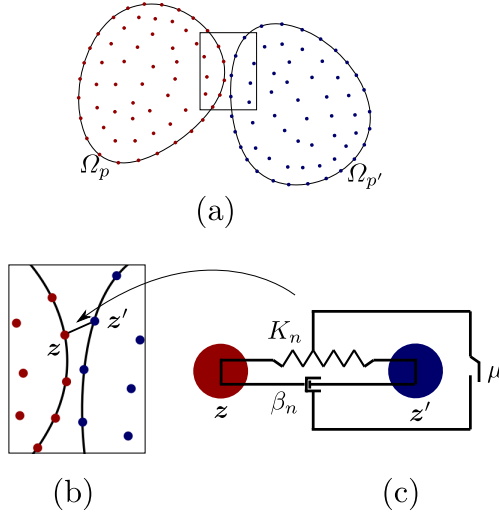


Figure 2: Schematics of contact forces on two particles Ω_p and $\Omega_{p'}$ in contact. In (a) we show the typical discretization of both particles. Here red and blue points are discrete nodes within particles 1 and 2. In (b) we zoom the region where contact forces are in play. In (c) we show typical contact forces acting between nodes \mathbf{x}, \mathbf{x}' at current positions \mathbf{z}, \mathbf{z}' .

2.2.1. Normal contact force

We assume that the points \mathbf{x}, \mathbf{x}' at current position \mathbf{z}, \mathbf{z}' are connected by a linear spring with following properties:

- K_n is the spring constant
- R_c is the equilibrium length (contact radius)
- The spring does not resist tensile loading.

Let δ is the spring stretch defined as the change in the length of spring relative to the equilibrium length, i.e,

$$\delta(\mathbf{z}, \mathbf{z}') = |\mathbf{z} - \mathbf{z}'| - R_c. \quad (16)$$

Then the density of the normal contact force on \mathbf{x} due to \mathbf{x}' is given by

$$\mathbf{F}_n(\mathbf{x}', \mathbf{x}) = \begin{cases} K_n \delta(\mathbf{z}, \mathbf{z}') V' \mathbf{e}_n, & \text{if } \delta(\mathbf{z}, \mathbf{z}') < 0, \\ \mathbf{0} & \text{otherwise,} \end{cases} \quad (17)$$

where \mathbf{e}_n is the unit vector pointing at \mathbf{z}' from \mathbf{z} ie

$$\mathbf{e}_n = \frac{\mathbf{z}' - \mathbf{z}}{|\mathbf{z}' - \mathbf{z}|}. \quad (18)$$

The spring modulus K_n can be related to the bulk modulus of the material in contact, see [subsection 3.1](#).

2.2.2. Frictional force

The friction force on contacting particles act on a plane with normal \mathbf{e}_n . The direction of force is given by

$$\mathbf{e}_t = [\mathbf{I} - \mathbf{e}_n \otimes \mathbf{e}_n] \frac{\mathbf{v}' - \mathbf{v}}{|\mathbf{v}' - \mathbf{v}|}, \quad (19)$$

where $\frac{\mathbf{v}' - \mathbf{v}}{|\mathbf{v}' - \mathbf{v}|}$ is unit vector along the relative velocity of impacting points. Here $\mathbf{v} = \mathbf{v}(\mathbf{x}, t)$ and $\mathbf{v}' = \mathbf{v}(\mathbf{x}', t)$ are velocities of points \mathbf{x}, \mathbf{x}' . The friction force on \mathbf{x} due to \mathbf{x}' is given by (Coulomb's law)

$$\mathbf{F}_t(\mathbf{x}', \mathbf{x}) = -\mu |\mathbf{F}_n(\mathbf{x}', \mathbf{x})| \mathbf{e}_t. \quad (20)$$

2.3. Damping force

For damping we consider two models. In the first model, damping force is defined similar to normal contact force. In the second model, the damping force is applied between the centroid of two contacting particles.

2.3.1. Damping force between material points

In addition to spring between point \mathbf{x}, \mathbf{x}' , we now suppose there is a dashpot with following properties

- β_n is viscosity of the dashpot
- Damping force is linear with rate of change in spring length $\dot{\delta}$ given by

$$\dot{\delta} = \frac{d}{dt} \delta(\mathbf{z}, \mathbf{z}') = (\mathbf{v}' - \mathbf{v}) \cdot \frac{\mathbf{z}' - \mathbf{z}}{|\mathbf{z}' - \mathbf{z}|} \quad (21)$$

- Damping force is zero when $\delta(\mathbf{z}, \mathbf{z}') > 0$.

The density of damping force on \mathbf{x} is then given by

$$\mathbf{F}_d(\mathbf{x}', \mathbf{x}) = \begin{cases} -\frac{1}{V} \beta_n \dot{\delta}(\mathbf{z}, \mathbf{z}') \mathbf{e}_n, & \text{if } \delta(\mathbf{z}, \mathbf{z}') < 0, \\ \mathbf{0} & \text{otherwise.} \end{cases} \quad (22)$$

The viscosity parameter β_n is based on the empirical formula (see Desai [2], Desai et al. [30])

$$\beta_n = -2C \log(\varepsilon_n) \sqrt{\frac{K_n m_{eq}}{\pi^2 + \log(\varepsilon_n)^2}}, \quad (23)$$

where m_{eq} is the Harmonic mean of the mass of two nodes in contact ie

$$m_{eq} = \frac{2\rho V \rho' V'}{\rho V + \rho' V'}, \quad (24)$$

where we recall that V, V' are nodal volumes and ρ, ρ' mass density of two nodes in contact. K_n is the spring modulus in Equation 17, the parameter $\varepsilon_n \leq 1$ controls the damping effect, and $C > 0$ is a constant.

2.3.2. Damping force between particle centers

Alternatively, we can apply the damping between the particle centers. Suppose \mathbf{x}_c and \mathbf{x}'_c are centers of particles in contact, $\mathbf{z}_c, \mathbf{z}'_c$ current position of the particle centers, and $\mathbf{v}_c, \mathbf{v}'_c$ velocity at the centers. We model the damping using dashpot between \mathbf{x}_c and \mathbf{x}'_c with following properties:

- $\bar{\beta}_n$ is viscosity of the dashpot
- $\dot{\delta}_c$ is the rate of change in the length given by

$$\dot{\delta}_c = (\mathbf{v}'_c - \mathbf{v}_c) \cdot \frac{\mathbf{z}'_c - \mathbf{z}_c}{|\mathbf{z}'_c - \mathbf{z}_c|} \quad (25)$$

- Damping force acts only when the distance, $dist(\Omega_p, \Omega_{p'})$, between particles is less than contact radius R_c .

The density of total damping force at the center of particle Ω_p due to $\Omega_{p'}$ in this case is given by

$$\bar{\mathbf{F}}_d(\mathbf{x}'_c, \mathbf{x}_c) = \begin{cases} -\frac{1}{|\Omega_p|} \bar{\beta}_n \dot{\delta}_c \frac{\mathbf{z}'_c - \mathbf{z}_c}{|\mathbf{z}'_c - \mathbf{z}_c|}, & \text{if } dist(\Omega_p, \Omega_{p'}) < R_c, \\ \mathbf{0} & \text{otherwise.} \end{cases} \quad (26)$$

The parameter $\bar{\beta}_n$ similar to before and is given by

$$\bar{\beta}_n = -2\bar{C} \log(\bar{\varepsilon}_n) \sqrt{\frac{K_n M_{eq}}{\pi^2 + \log(\bar{\varepsilon}_n)^2}}, \quad (27)$$

where M_{eq} is the Harmonic mean of the mass of two particles in contact ie

$$M_{eq} = \frac{2\rho |\Omega_p| \rho' |\Omega_{p'}|}{\rho |\Omega_p| + \rho' |\Omega_{p'}|}, \quad (28)$$

Here $|\Omega_p|$ denotes the volume (area in 2d) of the domain. K_n is normal contact parameter in [Equation 17](#), $\bar{\varepsilon}_n \leq 1$ as before controls the damping effect, and \bar{C} is a prescribed constant.

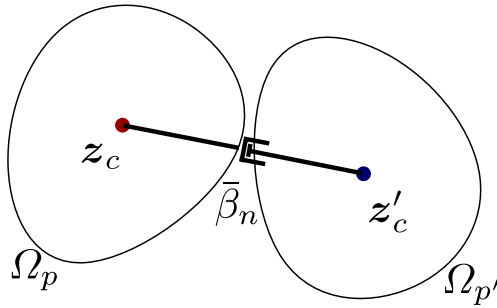


Figure 3: Model of damping acting between the centroid of particles.

Since $\bar{\mathbf{F}}(\mathbf{x}'_c, \mathbf{x}_c)$ is the density of total force acting on the particle center, the force density on individual nodes $\mathbf{x} \in \Omega_p$ is given by

$$\mathbf{F}_d(\mathbf{x}) = \bar{\mathbf{F}}_d(\mathbf{x}'_c, \mathbf{x}_c). \quad (29)$$

This completes the description of the inter-particle contact forces. We now present applications of the model.

3. Numerical tests

In this section, we apply the model to thoroughly examine two and multi-particle systems and highlight key features. First, we apply the model to a two-particle setup and show the damping effects. Next, we study the effect of mesh size on the model behavior. We then use the model to simulate a compressive test. Here 25 particles are confined into a rectangular domain with the top wall moving towards the particles at a prescribed speed that results in a compressive force applied to the collection of particles. Before presenting the results, we discuss the key implementation details of the *PeriDEM* method.

3.1. PeriDEM implementation

Peridynamics is typically discretized using a particle mesh defined as the set of pairs of nodes \mathbf{x}_i and the nodal volume V_i . We utilize the Gmsh library Geuzaine and Remacle [37] for triangulation of the particle and wall. From the unstructured mesh, we obtain the particle mesh, see [Figure 4](#). Consider a 2 dimensional problem with mesh consisting of triangular elements. There are two approaches to obtain the particle mesh: 1. Taking the center of each triangle element as the node and the volume of element as the nodal volume. 2. Taking the vertices of the triangle as the node and computing the volume of each vertex using an interpolation function. We follow the method 2 and present steps to compute the nodal volume. Suppose ϕ_i , $i \in \{1, 2, \dots, N\}$, is the interpolation function associated to the vertex i . Also let N_i is the list of elements e in the mesh that has node i as the vertex. Then the volume represented by the vertex i is given by

$$V_i = \sum_{e \in N_i} \int_{T_e} \phi_i(\mathbf{x}) d\mathbf{x}, \quad (30)$$

where T_e is the element domain.

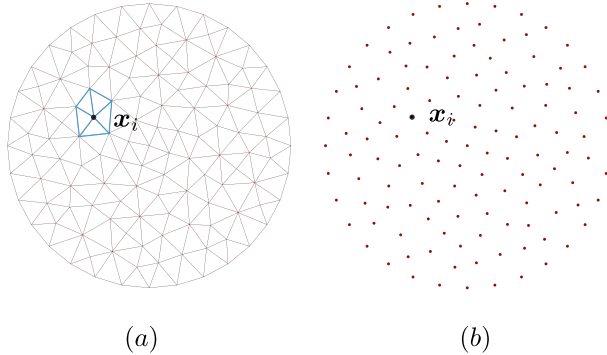


Figure 4: Discretization of particle. (a) Typical unstructured mesh of particle. (b) Corresponding particle mesh. In (a) and (b) we show generic vertex \mathbf{x}_i . In (a) the elements which have \mathbf{x}_i as vertex are highlighted.

For temporal discretization of [Equation 2](#), we consider a central-difference scheme. This results in following equation governing the evolution of the displacement of the node i :

$$\rho_i \frac{\mathbf{u}_i^{n+1} - 2\mathbf{u}_i^n + \mathbf{u}_i^{n-1}}{\Delta t^2} = \mathbf{F}_i + \mathbf{F}_{i,ext}, \quad (31)$$

where $\rho_i, \mathbf{u}_i, \mathbf{F}_i, \mathbf{F}_{i,ext}$ denotes density, displacement, internal force density, and contact and external force densities at node i . $\mathbf{F}_{i,ext}$ includes the contact forces due to contact of particle containing i with other particles. \mathbf{u}_i^n denotes the displacement of node i at time $t_n = n\Delta t$. \mathbf{F}_i is the approximation of the peridynamics force density on node i and is given by

$$\mathbf{F}_i = \sum_{\substack{j, |\mathbf{x}_j - \mathbf{x}_i| < \epsilon, \\ \mathbf{x}_j \neq \mathbf{x}_i}} (\mathbf{T}_{\mathbf{x}_i}(\mathbf{x}_j) - \mathbf{T}_{\mathbf{x}_j}(\mathbf{x}_i))V_j, \quad (32)$$

where $T_{\mathbf{x}_j}(\mathbf{x}_i)$ is the approximation of $T_{\mathbf{y}}(\mathbf{x})$, see [Equation 12](#) where T is defined. It depends on $\theta_{\mathbf{x}_i}$ and $m_{\mathbf{x}_i}$ which are approximately computed as follows:

$$\begin{aligned} m_{\mathbf{x}_i} &= \sum_{\substack{j, |\mathbf{x}_j - \mathbf{x}_i| < \epsilon, \\ \mathbf{x}_j \neq \mathbf{x}_i}} |\mathbf{x}_j - \mathbf{x}_i|^2 J(|\mathbf{x}_j - \mathbf{x}_i|/\epsilon)V_j, \\ \theta_{\mathbf{x}_i} &= \frac{3}{m_{\mathbf{x}_i}} \sum_{\substack{j, |\mathbf{x}_j - \mathbf{x}_i| < \epsilon, \\ \mathbf{x}_j \neq \mathbf{x}_i}} h(s(\mathbf{x}_j, \mathbf{x}_i), t)|\mathbf{x}_j - \mathbf{x}_i|(|\mathbf{z}(\mathbf{x}_j) - \mathbf{z}(\mathbf{x}_i)| - |\mathbf{x}_j - \mathbf{x}_i|)J(|\mathbf{x}_j - \mathbf{x}_i|/\epsilon)V_j. \end{aligned} \quad (33)$$

This completes the description of the discretization of peridynamics equation of motion. The following section provides details about the contact force calculation.

3.1.1. Contact parameter

We define the size of particle mesh as follows:

$$h = \min_{\substack{\mathbf{x}_i, \mathbf{x}_j \\ \mathbf{x}_i \neq \mathbf{x}_j}} |\mathbf{x}_i - \mathbf{x}_j|. \quad (34)$$

In all simulations we have fixed the contact radius using $R_c = 0.95h$. For the spring modulus K_n we use the formula Behzadinasab et al. [\[20\]](#), Silling and Askari [\[16\]](#)

$$K_n = \frac{18\kappa}{\pi\epsilon^5}, \quad (35)$$

where ϵ is the horizon and κ is the bulk modulus. In the case when the contacting particles have different bulk moduli κ_1 and κ_2 , we define K_n using an effective bulk modulus κ_{eff} given by

$$\kappa_{eff} = \frac{2\kappa_1\kappa_2}{\kappa_1 + \kappa_2}. \quad (36)$$

Now it remains to specify the damping parameter. In this work, we apply the damping between particle centers described in [subsubsection 2.3.2](#). In all simulations, we have fixed $\bar{C} = 100$. The value of the parameter $\bar{\varepsilon}_n$ is specific to the numerical example and will be discussed when describing the setup.

Intra-particle contact: Consider a pair of node $\mathbf{x}_i, \mathbf{x}_j \in \Omega$ with broken bond. To prevent self-penetration, we apply the normal contact force between such nodes \mathbf{x}_i and \mathbf{x}_j . Formula for the contact force is same as in [Equation 17](#) where K_n is computed from the bulk modulus as in [Equation 35](#). The contact radius is fixed by $R_c = 0.95h$.

3.2. Two-particle test

In this test, we consider two particles in which the particle at the bottom is fixed and rigid, and the particle on the top is falling due to gravity, see [Figure 5](#). We study the effect of damping parameter $\bar{\varepsilon}_n$ on the rebound height after the first contact. We take $g = 10 \text{ m/s}^2$ along the negative vertical direction as the gravity. If H_0 is the initial distance between the two particles and H_1 is the maximum distance after the first contact, the coefficient of restitution (CoR) is given by

$$C_R = \sqrt{\frac{H_1}{H_0}}. \quad (37)$$

$C_R = 1$ implies perfectly elastic collision whereas $C_R < 1$ implies loss of energy due to damping. C_R is specific to two materials in contact and is used to calibrate the damping coefficient $\bar{\varepsilon}_n$, see Desai [2], Desai et al. [30].

To demonstrate the effect of damping on the coefficient of restitution, we consider two different materials and perform tests where we combine the material type and vary the radius of the top and bottom particles. [Table 1](#) lists the material properties. Particles are discretized using Gmsh with mesh size $h = 0.1423 \text{ mm}$ where h is computed from [Equation 34](#). The horizon for the non-local model is fixed to $\epsilon = 0.6 \text{ mm}$. The total time of the simulation is $T = 0.04 \text{ s}$. The timestep size largely depends on the spring constant K_n . We consider $\Delta t = 0.2, 0.02 \mu\text{s}$ for tests with material M1 and M2 respectively. For the material pair (M1, M2), we consider $\Delta t = 0.1 \mu\text{s}$.

In [Table 2](#), we list the values of C_R for different damping parameter $\bar{\varepsilon}_n$ for particles of material M1 and radius $R_1 = R_2 = 1 \text{ mm}$. Naturally in the absence of damping we have elastic contact in which the top particle rebounds to the same height resulting in $C_R = 1$. In [Table 3](#) we list values of C_R for various tests for the case of elastic contact and contact with $\bar{\varepsilon}_n = 0.95$. For fixed parameter $\bar{\varepsilon}_n$, the effect of damping is smaller in the material with smaller strength. In all cases an increase in $\bar{\varepsilon}_n$ implies an increase in damping and therefore decrease in C_R . The simulation results for the cases Tables [Table 2](#) and [Table 3](#) are shown in [Figure 6](#)

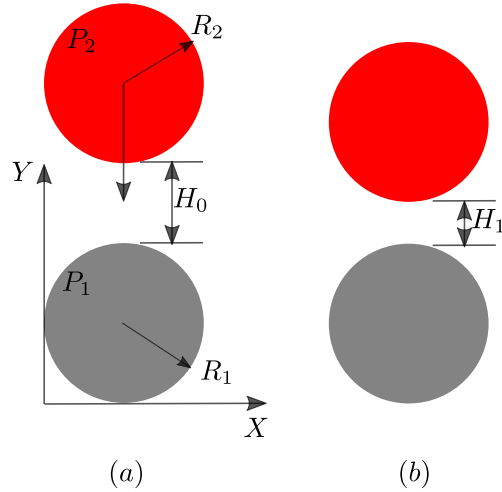


Figure 5: Two-particle test. (a) Initial state. Particle at the bottom is fixed and rigid whereas particle on top is dropped from the height H_0 with zero initial velocity. (b) Later time after the first contact when particle 2 has bounced to maximum height. H_1 is the relative distance after the contact.

| Material set | ρ | K | G | G_c |
|-----------------|------------------------|------------|-------------|----------------------|
| M1 | 1200 Kg/m ³ | 0.0216 GPa | 0.01296 GPa | 50 J/m ² |
| M2 (PMMA Glass) | 1200 Kg/m ³ | 2 GPa | 1.2 GPa | 500 J/m ² |

Table 1: Two sets of materials. Here ρ denotes density, K bulk modulus, G shear modulus, and G_c critical energy release rate.

| Test | $\bar{\varepsilon}_n$ | C_R |
|------|-----------------------|-------|
| 1 | 1 | 1 |
| 2 | 0.95 | 0.946 |
| 3 | 0.9 | 0.893 |
| 4 | 0.85 | 0.845 |
| 5 | 0.8 | 0.796 |

Table 2: Coefficient of restitution for two-particle test. Here $R_1 = R_2 = 1$ mm and material properties of both particles are same as M1 in [Table 1](#). Initial separation between particle H_0 is 1 mm. As $\bar{\varepsilon}_n$ increases C_R decreases. Further, for fixed $\bar{\varepsilon}_n$, the damping effect is smaller for material with smaller strength.

| Test | (R_1, R_2) | Material pair | C_R ($\bar{\varepsilon}_n = 1$) | C_R ($\bar{\varepsilon}_n = 0.95$) |
|------|--------------|---------------|-------------------------------------|--|
| 6 | (3,1) | (M1, M1) | 1 | 0.935 |
| 7 | (1,1) | (M2, M2) | 1 | 0.744 |
| 8 | (3,1) | (M2, M2) | 1 | 0.716 |
| 9 | (1,1) | (M2, M1) | 1 | 0.925 |
| 10 | (3,1) | (M2, M1) | 1 | 0.914 |

Table 3: Coefficient of restitution for mixed cases. We consider elastic collision and collision with $\bar{\varepsilon}_n = 0.95$. In all tests we have $H_0 = 1$ mm.

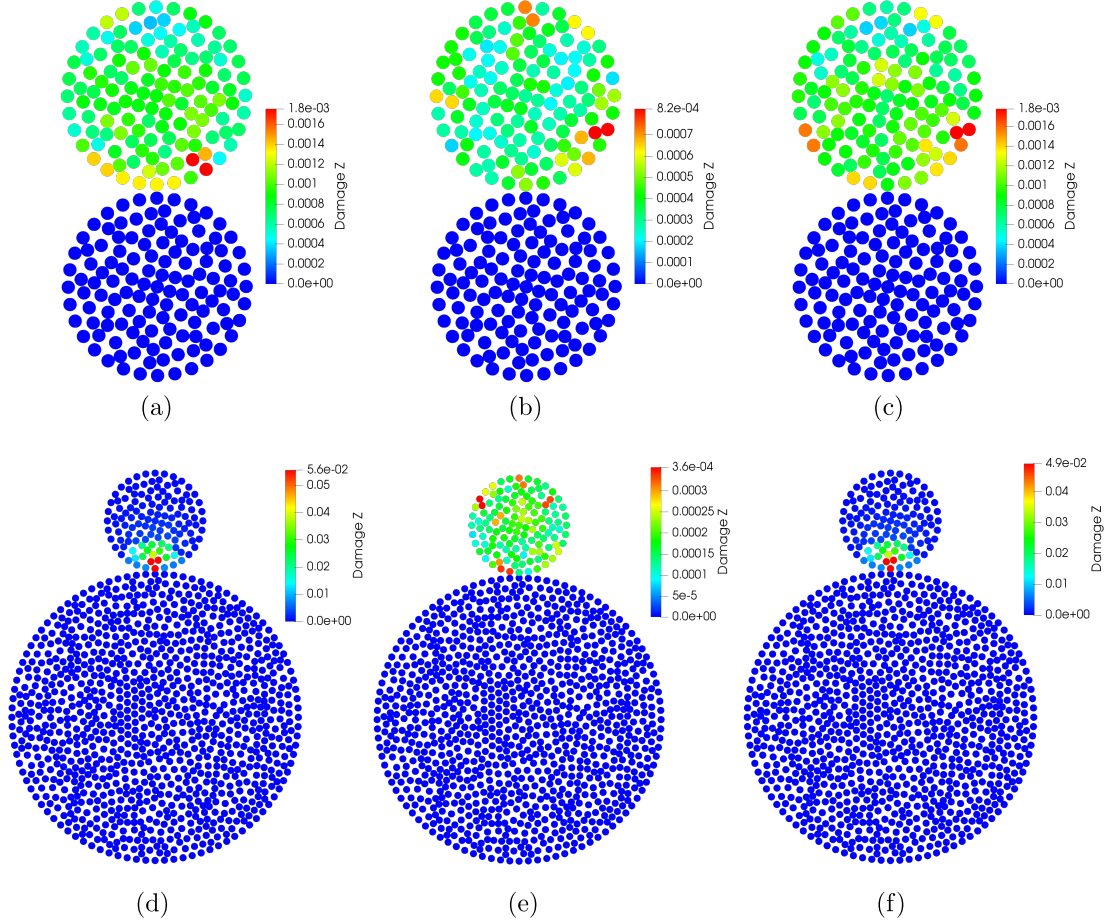


Figure 6: Plot of damage close to the contact time. Damage function Z is defined in [Equation 14](#). $Z(\mathbf{x}) < 1$ implies no fracture whereas $Z(\mathbf{x}) \geq 1$ implies one or more bonds in the neighborhood of point \mathbf{x} is broken. All plots correspond to same time $t = 0.0044$ s. (a) and (b) correspond to test 1 and 2 with $\bar{\varepsilon}_n = 0.95$ in [Table 2](#). (c), (d), (e), (f) corresponds to test 9, 6, 8, 10 respectively in [Table 3](#).

Fracture simulations. We assign initial downward velocity v_0 to the top particle in [Figure 5](#). As the velocity increases, the damage near the contact area increases and eventually at high enough velocities, the downward falling particle breaks. In [Figure 7](#), we show plot of damage just after the contact for different values of v_0 in test 2 [Table 2](#). The evolution of top particle for the case of $v_0 = 5$ m/s at four times is presented in [Figure 8](#). For the same range of velocities, we considered test 10 in [Table 3](#) with $\bar{\varepsilon}_n = 0.95$. The damage plots for this case are shown in [Figure 9](#) and evolution of top particle for the case of $v_0 = 5$ m/s is presented in [Figure 10](#).

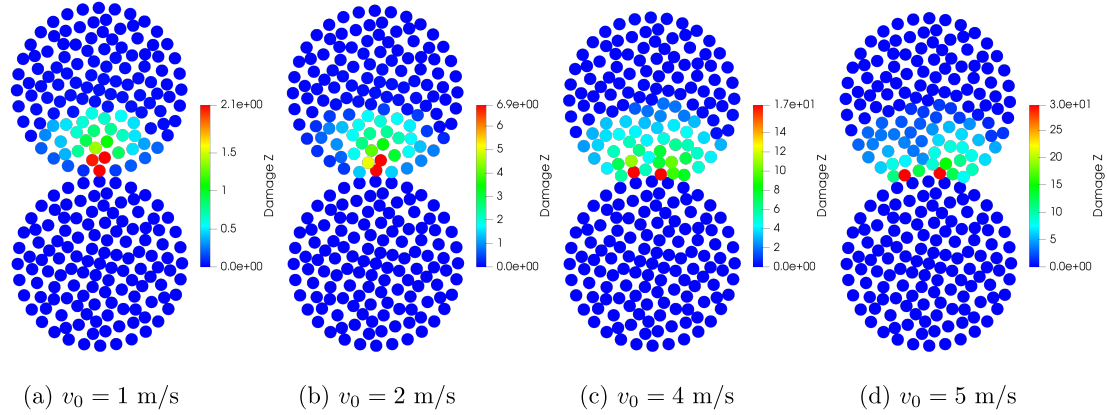


Figure 7: Plot of damage for two-particle test 2 in Table 2. v_0 is the initial velocity of top particle along downward direction. Final time and time step for all four cases are $T = 0.001 \text{ s}$ and $\Delta t = 0.2 \mu\text{s}$. For all cases, the fracture zone FZ is present ie there are nodes such that $Z(\mathbf{x}) \geq 1$.

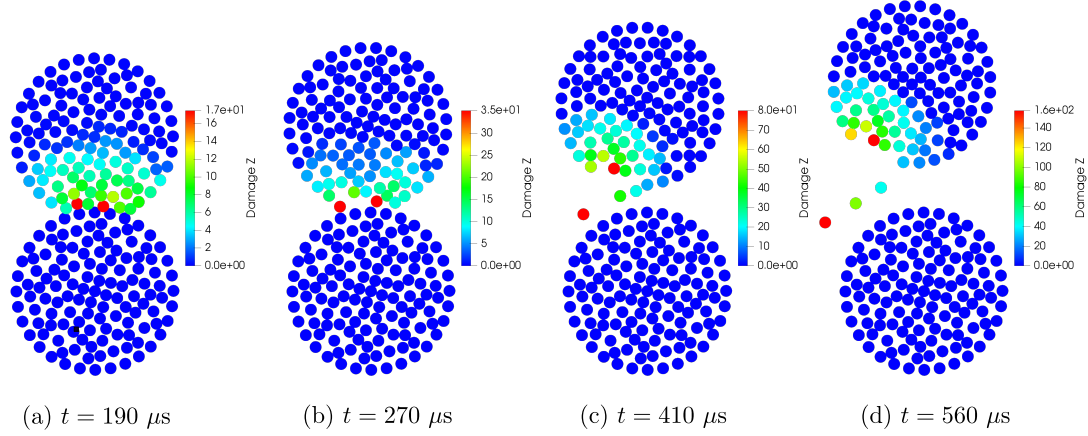


Figure 8: Particle evolution at 4 different times. The results correspond to test 2 in Table 2 with $v_0 = 5 \text{ m/s}$.

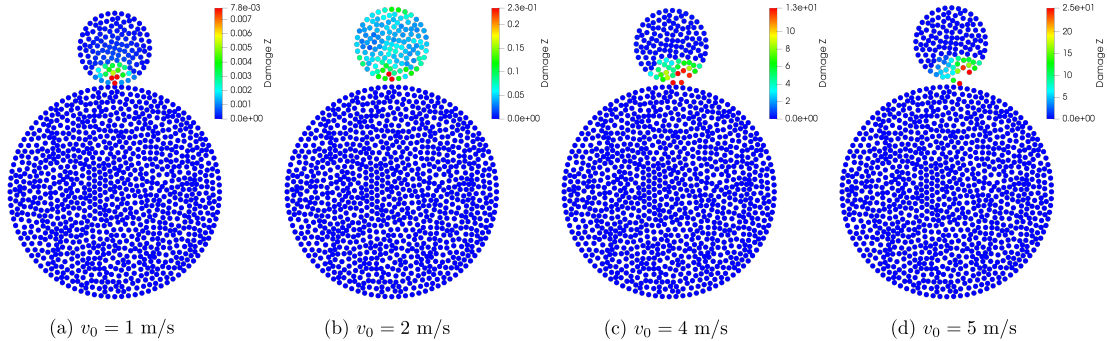


Figure 9: Plot of damage for two-particle test 10 ($\bar{\varepsilon}_n = 0.95$) in Table 3. Final time and time step for all four cases are $T = 0.001 \text{ s}$ and $\Delta t = 0.1 \mu\text{s}$.

| Test | Mesh size (mm) | Horizon (mm) | Δt (μs) | H_0 (mm) | C_R ($\bar{\varepsilon}_n = 1$) | C_R ($\bar{\varepsilon}_n = 0.95$) |
|------|----------------|--------------|------------------------------|------------|-------------------------------------|--|
| 1 | 0.1423 | 0.6 | 0.2 | 1 | 1 | 0.946 |
| 2 | 0.0805 | 0.375 | 0.1 | 1 | 1 | 0.962 |
| 3 | 0.062 | 0.3 | 0.1 | 1 | 1 | 0.968 |
| 4 | 0.0379 | 0.2 | 0.05 | 1 | 1 | 0.977 |

Table 4: C_R for the case when particles have the same radius $R = 1$ mm and have same material properties M1. As mesh size h decreases, the contact radius $R_c = 0.95h$ also decreases resulting in smaller area of contact and smaller duration of contact. This results in smaller damping effect as the mesh size is reduced. For small horizon, peridynamics material behaves more like a brittle material which may also contribute to the smaller damping effect when the mesh size is small.

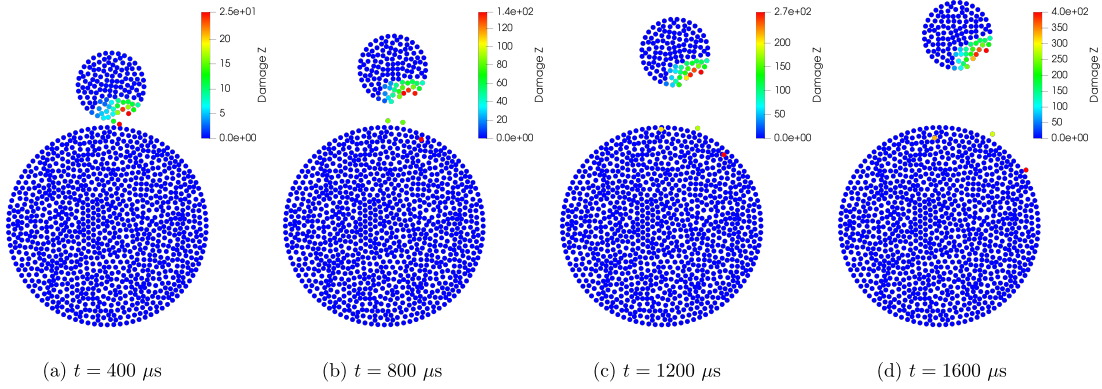


Figure 10: Particle evolution at 4 different times. The results correspond to test 10 ($\bar{\varepsilon}_n = 0.95$) in [Table 3](#) with $v_0 = 5$ m/s.

3.2.1. Mesh effect

Consider test 2 in [Table 2](#). To see how the model behaves with different grid or mesh sizes, we consider 4 meshes of decreasing mesh size and horizon, and record the C_R . C_R is listed in [Table 4](#). As mentioned in [subsection 3.1](#), the contact radius depends on mesh size via $R_c = 0.95h$. Thus with decreasing mesh size, the size of contact neighborhood decreases. Duration for which damping is effective depends on the contact neighborhood and therefore with smaller mesh size, the reduced damping effect is seen in [Table 4](#). The damage in the material near the impact time is shown in [Figure 12](#).

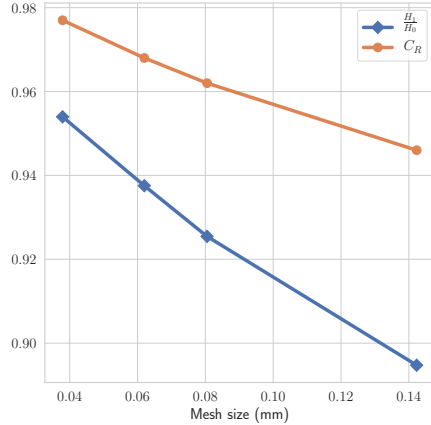


Figure 11: C_R for different mesh sizes. Here as mesh size reduces, the contact radius also reduces following formula $R_c = 0.95h$. We expect with decreasing mesh the smaller damping effect due to reduction in the contact area and reduction in the contact duration.

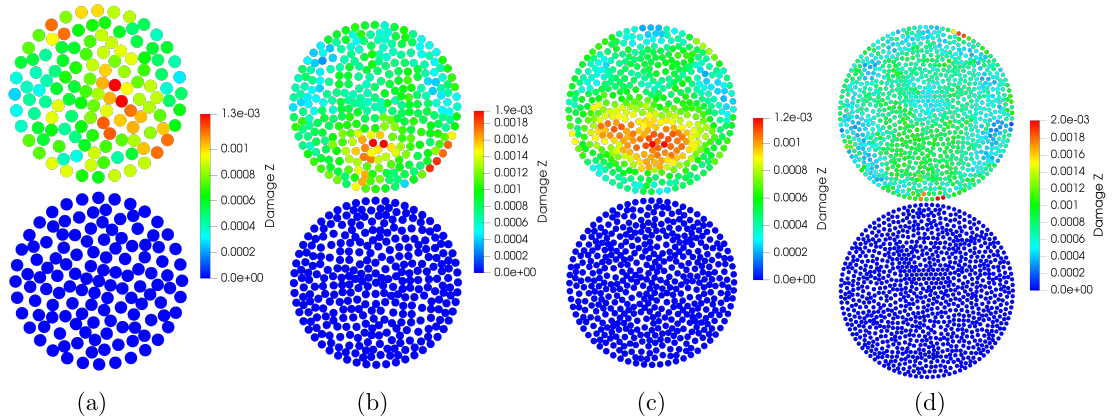


Figure 12: Plot of damage for tests in [Table 4](#). Note that magnitude of damage is of the same order for all four simulations.

3.3. Two-particle with wall

We consider a setup similar to [subsection 3.2](#) but now with a fixed wall below the bottom particle. The setup shown in [Figure 13](#) consists of two particles of different radii and materials. The bottom particle is free falling where as the top particle is assigned an initial velocity v_0 .

Both particles and wall made-up of the same material M1. We take $R_1 = 1$ mm, $R_2 = 2$ mm, $H_0 = 1$ mm. The mesh size is $h = 0.1423$ mm and horizon is $\epsilon = 0.6$ mm. Final simulation time is $T = 0.04$ s and the time step is $\Delta t = 0.1 \mu\text{s}$. Damping parameter $\bar{\varepsilon}_n$ is fixed to 0.95. We consider three different initial velocities $v_0 = 2, 4, 5$ m/s. The damage at the impact time for all three cases is shown in [Figure 14](#). Evolution of particles for the case when $v_0 = 5$ m/s is shown in [Figure 15](#). Since both particles have same material strength, the fracture is seen on both particles. Region containing points with broken bonds in the neighborhood (fracture zone FZ , see [Equation 15](#)) increases with increasing v_0 .

Particles and wall made-up of different materials. For top particle and the fixed wall, we consider material M2 with higher strength. For particle in between wall and top particle, we consider material M1. Other parameters are same as before. The damage at the impact time for three different initial velocities $v_0 = 2, 4, 5 \text{ m/s}$ is shown in Figure 16. Evolution of particles for the case when $v_0 = 5 \text{ m/s}$ is shown in Figure 17. Note that only bottom particle breaks while top particle remains intact. This is expected as the top particle has higher strength.

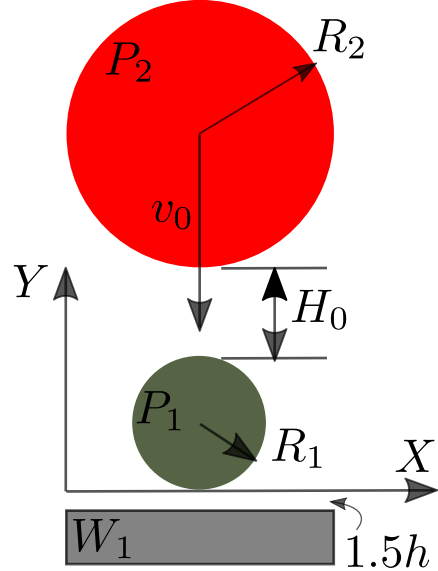


Figure 13: Schematics of two-particle with wall test. Here both particles are falling freely due to gravity $g = 10 \text{ m/s}^2$ in downward direction. The wall is fixed in place. P_2 is given an initial velocity of v_0 downwards.

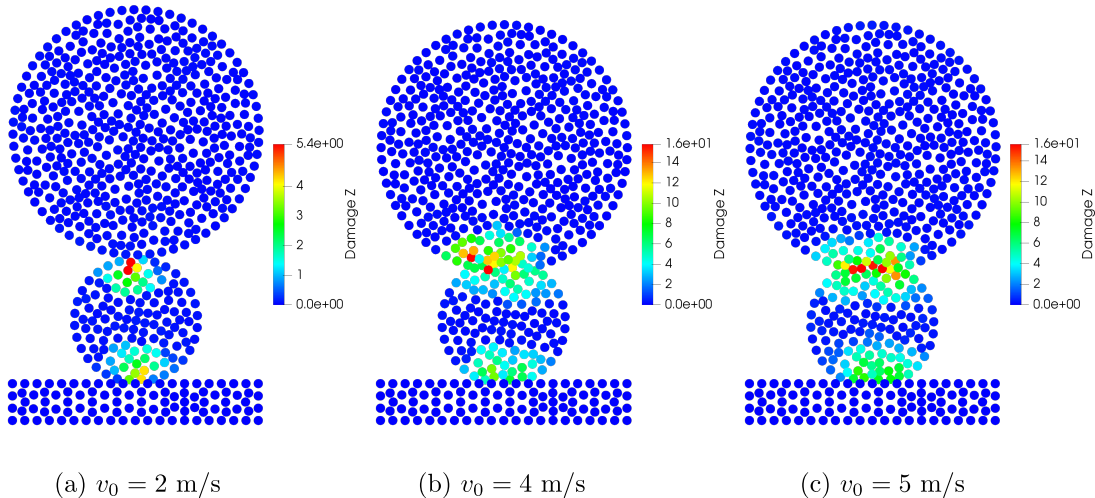


Figure 14: Plot of damage when particles and wall have same material properties. Since both particle have same strength and critical energy release rate, both particles break.

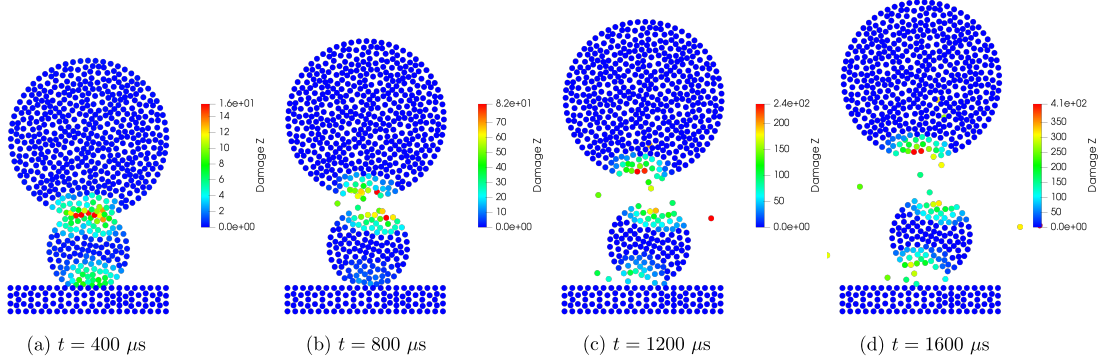


Figure 15: Evolution of particles for test with same material properties for the case of $v_0 = 5 \text{ m/s}$. Since both particle have same strength and critical energy release rate, both particles break.

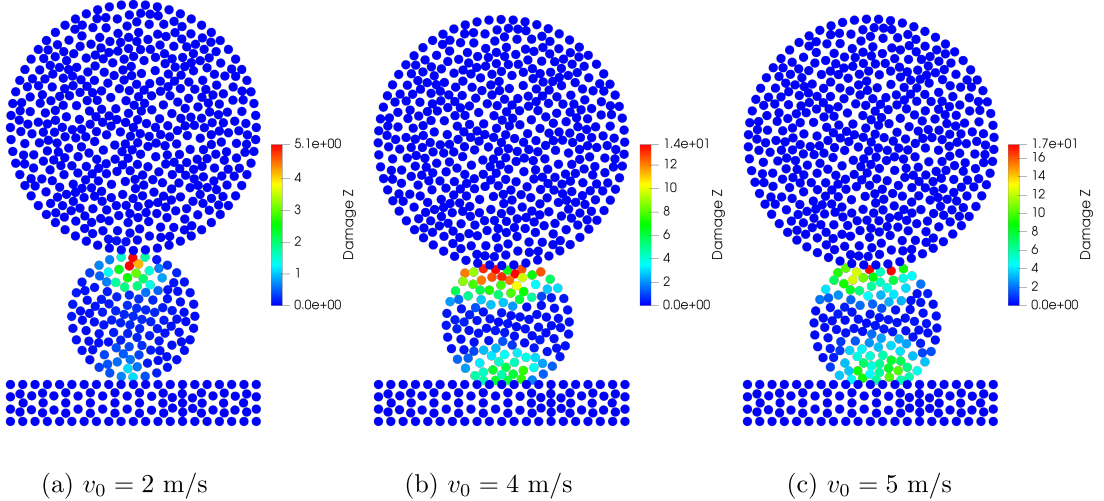


Figure 16: Plot of damage when particles and wall have different material properties. Wall and top particle has material property M2 whereas bottom particle has material property M1. Since the top particle has higher strength and higher critical energy release rate compared to the bottom particle, only bottom particle breaks.

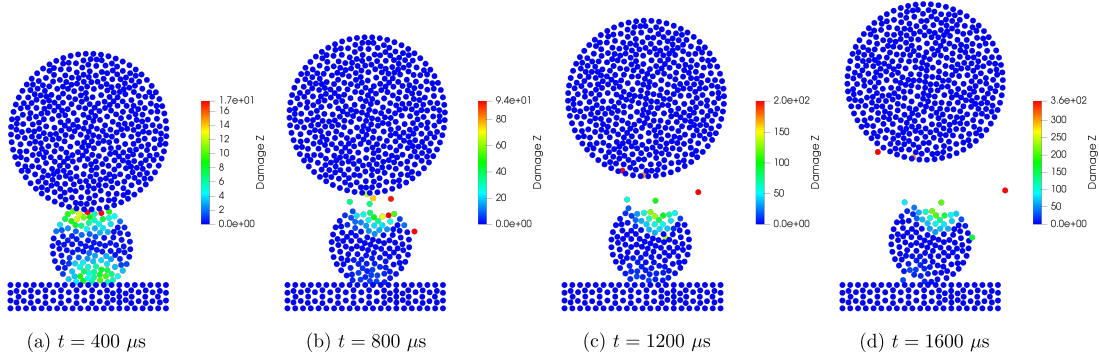


Figure 17: Evolution of particles for test with different material properties and initial velocity $v_0 = 5$ m/s of top particle. Note that the top particle is undamaged (no nodes with $Z \geq 1$) as it has higher strength.

3.4. Multi-particle compressive test

So far, we have shown the application of the model to settings involving two particles. Two-particle settings provide useful information and allow one to calibrate the contact parameters for the desired effect. Further, these serve the purpose of code validation and verification. Our results show that the model can be calibrated for damping effects and behaves consistently with varying parameters such as particle radius and material properties. Thus far, the applications also highlight the features of the model to seamlessly capture inter-particle dynamics and intra-particle damage that may eventually result in total breakage under certain conditions.

In this section, we consider a slightly more complex setting involving 25 particles of varying radii in a rectangular container, see Figure 18. The top wall of the container is moving inwards at a constant velocity. Media is subjected to gravity $g = 10$ m/s² downwards. Particle radius is based on a normal distribution $R \sim 1 + \mathcal{U}(-0.1, 0.1)$ where units are in mm. Further, the particles are randomly perturbed in x-direction a little so that the centers of particles are not aligned vertically. Figure 18 shows other geometric details and the velocity of the top wall. Walls and particles are discretized using Gmsh library, and later the mesh is converted to the particle mesh following subsection 3.1. Mesh size of the discretization of particle with radius $R = 1$ mm is 0.1423 mm. Final simulation time is $T = 0.06$ s and the size of time step is $\Delta t = 0.2$ μ s.

In Figure 19, we plot the configuration of the particles and the intra-particle damage at different times. The results show that the damage initiates near the contact point and then reaches inwards. Initially, particles adjust as the wall begins to exert force on the topmost particles; see Figure 19(a) and (b). The particle interlocking and the subsequent formation of the force-chains is seamlessly captured by this model. As the load from the moving wall increases, see Figure 19(c) onward, the damage in particles begins to spread to the inside indicating particulate media has yielded due to fracture in individual particles. Significant particle damage, attritions, and eventual breakage is seen at the end of the simulation, see Figure 19(f).

In Figure 20, we plot the total reaction force (vertical component) on moving wall with respect to the wall penetration. We identify 4 points on the force curve and plot the configuration of particles with damage. We see that at time t_3 , the media yields a little due to the softening of the particles forming the force chain, see figure on right in Figure 20. The proposed model has potential application in estimation of the effective strength of the particulate media.

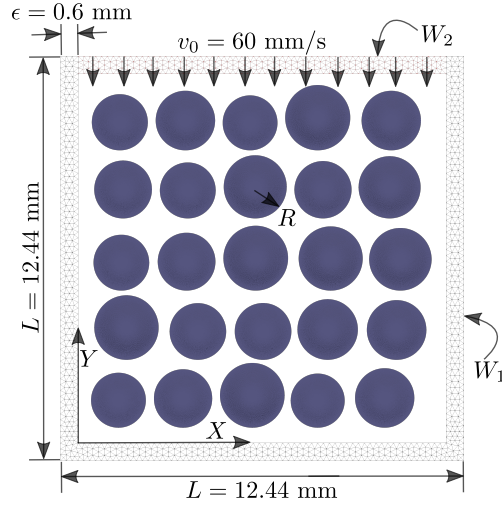


Figure 18: Multi-particle compressive test setup. Wall W_2 on top is moving downwards with constant velocity v_0 whereas W_1 comprising of vertical walls and bottom wall is fixed. Particles are subjected to gravity of $g = 10 \text{ m/s}^2$ downwards. Particle radii follow distribution $R \sim 1 + \mathcal{U}(-0.1, 0.1)$ (in units of mm) where $\mathcal{U}(a, b)$ is uniform distribution in interval $[a, b]$. Centers of particles are arranged in uniform grid. To not let particle centers aligned vertically, we randomly perturb the particles in the x-direction.

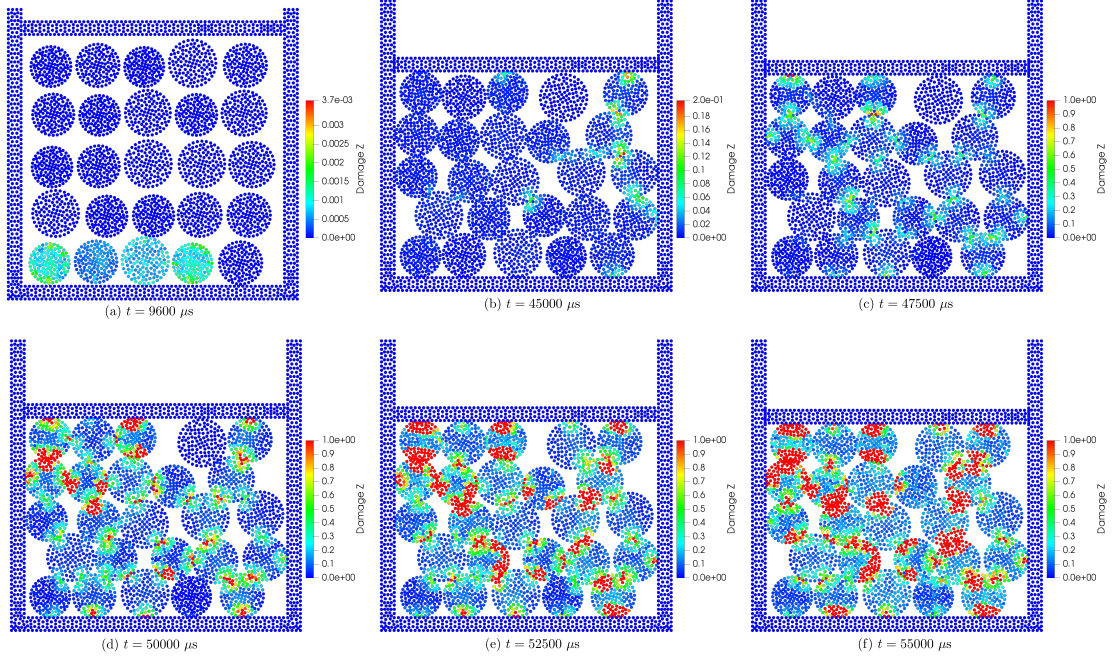


Figure 19: Damage on particles at different times. (a) Particles have begun to settle down and the top wall is yet to touch the topmost particles. (b) The top wall has now started exerting compressive force on the particle assembly. We also see the formation of force-chains and interlocking of particles. Damage begins from (c). From figure (c) onward, we fix the upper value of damage to 1 to see how damage progresses in the medium and in each particle. Note that damage $Z \geq 1$ indicates the node has one or more bonds in broken state in the neighborhood. Starting from damage at contact points in (c), we see damage has reached almost half of the radius inside particles in (f).

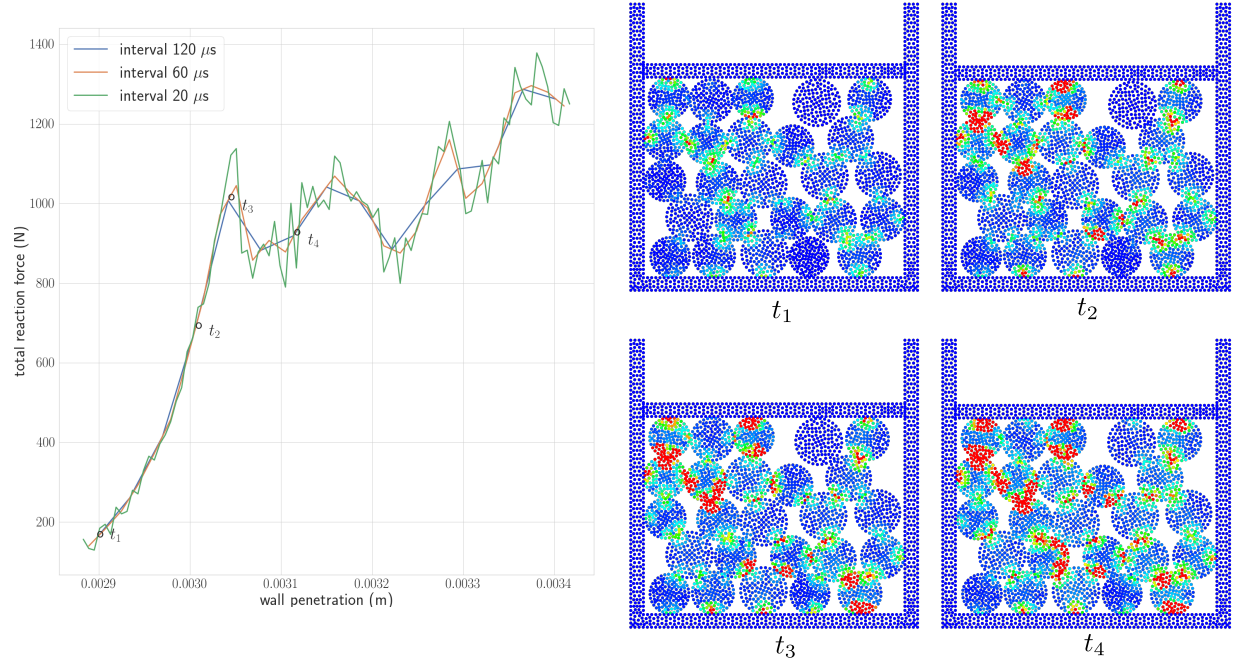


Figure 20: Left: Plot of downward wall distance vs reaction force (vertical component). We average the force using three different time intervals. This smoothes out the fluctuations in force due to the dynamic nature of the simulation. Right: Configuration with damage at particles at four times $\{48000, 49800, 50400, 51600\} \mu s$.

4. Conclusion

The authors have presented a new hybrid model that combines the advantages of the discrete element method (DEM) and peridynamics for more accurate simulations of the granular media. Numerical results show that the model is reliable under different scenarios, and parameters can be tuned to have the desired damping effect and contact stiffness. Under small deformation, the model behaves like an elastic body. However, situations such as high-velocity impacts, compressive loading from the surrounding walls, etc, can cause significant damage and attrition in the particles and ultimately result in particle breakage. When spherical particles break, they no longer maintain a convex geometry, and the resulting inter-particle locking may become important to capture particle dynamics accurately. The proposed model can seamlessly handle this scenario as the contact forces do not explicitly depend on the surface geometry of particles and these are applied at the local level. The model also correctly simulates the coefficient of restitution (CoR) in a two-particle impact test. A multi-particle compressive test shows the utility of the model to simulate particle wear and attrition. However, this added fidelity comes at higher computational costs. Future works will be towards engineering applications where particle deformation and particle fracture can play a major role in developing novel methods that reduce the computational costs arising from the nonlocal peridynamics and nonlocal contact force calculations.

References

- [1] P. A. Cundall, O. D. Strack, A discrete numerical model for granular assemblies, *geotechnique* 29 (1979) 47–65.
- [2] P. S. Desai, Tribosurface Interactions involving Particulate Media with DEM-calibrated Properties: Experiments and Modeling, Ph.D. thesis, Carnegie Mellon University, 2017.
- [3] C. Labra, E. Onate, High-density sphere packing for discrete element method simulations, *Communications in Numerical Methods in Engineering* 25 (2009) 837–849.
- [4] Z. Yan, S. K. Wilkinson, E. H. Stitt, M. Marigo, Investigating mixing and segregation using discrete element modelling (dem) in the freeman ft4 rheometer, *International journal of pharmaceutics* 513 (2016) 38–48.
- [5] Y. Feng, K. Han, D. Owen, Coupled lattice boltzmann method and discrete element modelling of particle transport in turbulent fluid flows: Computational issues, *International Journal for Numerical Methods in Engineering* 72 (2007) 1111–1134.
- [6] H. Zhu, Z. Zhou, R. Yang, A. Yu, Discrete particle simulation of particulate systems: theoretical developments, *Chemical Engineering Science* 62 (2007) 3378–3396.
- [7] A. Neveu, R. Artoni, P. Richard, Y. Descantes, Fracture of granular materials composed of arbitrary grain shapes: A new cohesive interaction model, *Journal of the Mechanics and Physics of Solids* 95 (2016) 308–319.
- [8] N. H. Nguyen, H. H. Bui, G. D. Nguyen, J. Kodikara, A cohesive damage-plasticity model for dem and its application for numerical investigation of soft rock fracture properties, *International Journal of Plasticity* 98 (2017) 175–196.
- [9] S. A. Silling, Reformulation of elasticity theory for discontinuities and long-range forces, *Journal of the Mechanics and Physics of Solids* 48 (2000) 175–209.
- [10] S. Silling, O. Weckner, E. Askari, F. Bobaru, Crack nucleation in a peridynamic solid, *International Journal of Fracture* 162 (2010) 219–227.
- [11] J. T. Foster, S. A. Silling, W. Chen, An energy based failure criterion for use with peridynamic states, *International Journal for Multiscale Computational Engineering* 9 (2011).
- [12] F. Bobaru, W. Hu, The meaning, selection, and use of the peridynamic horizon and its relation to crack branching in brittle materials, *International journal of fracture* 176 (2012) 215–222.
- [13] R. Lipton, Cohesive dynamics and brittle fracture, *Journal of Elasticity* 124 (2016) 143–191.
- [14] R. P. Lipton, R. B. Lehoucq, P. K. Jha, Complex fracture nucleation and evolution with nonlocal elastodynamics, *Journal of Peridynamics and Nonlocal Modeling* 1 (2019) 122–130.
- [15] P. K. Jha, R. P. Lipton, Kinetic relations and local energy balance for lefm from a nonlocal peridynamic model, *International Journal of Fracture* (2020) 1–15.
- [16] S. A. Silling, E. Askari, A meshfree method based on the peridynamic model of solid mechanics, *Computers & structures* 83 (2005) 1526–1535.
- [17] S. A. Silling, F. Bobaru, Peridynamic modeling of membranes and fibers, *International Journal of Non-Linear Mechanics* 40 (2005) 395–409.
- [18] Y. D. Ha, F. Bobaru, Studies of dynamic crack propagation and crack branching with peridynamics, *International Journal of Fracture* 162 (2010) 229–244.
- [19] P. Diehl, R. Lipton, M. Schweitzer, Numerical verification of a bond-based softening peridynamic model for small displacements: Deducing material parameters from classical linear theory, *Institut für Numerische Simulation Preprint* (2016).
- [20] M. Behzadinasab, T. J. Vogler, A. M. Peterson, R. Rahman, J. T. Foster, Peridynamics modeling of a shock wave perturbation decay experiment in granular materials with intra-granular fracture, *Journal of Dynamic Behavior of Materials* 4 (2018) 529–542.
- [21] R. Lipton, E. Said, P. Jha, Free damage propagation with memory, *Journal of Elasticity* 133 (2018) 129–153.
- [22] P. Wu, J. Zhao, Z. Chen, F. Bobaru, Validation of a stochastically homogenized peridynamic model for quasi-static fracture in concrete, *Engineering Fracture Mechanics* (2020) 107293.
- [23] Z. Chen, F. Bobaru, Peridynamic modeling of pitting corrosion damage, *Journal of the Mechanics and Physics of Solids* 78 (2015) 352–381.
- [24] S. Jafarzadeh, Z. Chen, S. Li, F. Bobaru, A peridynamic mechano-chemical damage model for stress-assisted corrosion, *Electrochimica Acta* 323 (2019) 134795.
- [25] Y. Zhang, S. Haeri, Y. Zhang, G. Pan, A coupled peridynamics and dem-ib-clbm method for sand erosion prediction in a viscous fluid, in: 6th European Conference on Computational Mechanics and 7th European Conference on Computational Fluid Dynamics 2018, 2018.
- [26] A. Katiyar, J. T. Foster, H. Ouchi, M. M. Sharma, A peridynamic formulation of pressure driven convective fluid transport in porous media, *Journal of Computational Physics* 261 (2014) 209–229.

- [27] H. Ouchi, A. Katiyar, J. York, J. T. Foster, M. M. Sharma, A fully coupled porous flow and geomechanics model for fluid driven cracks: a peridynamics approach, *Computational Mechanics* 55 (2015) 561–576.
- [28] R. P. Lipton, P. K. Jha, Nonlocal elastodynamics and fracture, arXiv preprint arXiv:2001.00313v3 (2020). URL: <https://arxiv.org/abs/2001.00313v3>.
- [29] F. Zhu, J. Zhao, Modeling continuous grain crushing in granular media: a hybrid peridynamics and physics engine approach, *Computer Methods in Applied Mechanics and Engineering* 348 (2019) 334–355.
- [30] P. S. Desai, A. Mehta, P. S. Dougherty, C. F. Higgs III, A rheometry based calibration of a first-order dem model to generate virtual avatars of metal additive manufacturing (AM) powders, *Powder Technology* 342 (2019) 441–456.
- [31] B. Asmar, P. Langston, A. Matchett, J. Walters, Validation tests on a distinct element model of vibrating cohesive particle systems, *Computers & chemical engineering* 26 (2002) 785–802.
- [32] P. K. Jha, R. Lipton, Numerical analysis of nonlocal fracture models in holder space, *SIAM Journal on Numerical Analysis* 56 (2018) 906–941.
- [33] S. A. Silling, M. Epton, O. Weckner, J. Xu, E. Askari, Peridynamic states and constitutive modeling, *Journal of Elasticity* 88 (2007) 151–184.
- [34] T. L. Warren, S. A. Silling, A. Askari, O. Weckner, M. A. Epton, J. Xu, A non-ordinary state-based peridynamic method to model solid material deformation and fracture, *International Journal of Solids and Structures* 46 (2009) 1186–1195.
- [35] F. Zhu, J. Zhao, A peridynamic investigation on crushing of sand particles, *Géotechnique* 69 (2019) 526–540.
- [36] D. J. Littlewood, M. L. Parks, J. A. Mitchell, S. A. Silling, The Peridigm Framework for Peridynamic Simulations., Technical Report, Sandia National Lab.(SNL-NM), Albuquerque, NM (United States), 2013.
- [37] C. Geuzaine, J.-F. Remacle, Gmsh: A 3-d finite element mesh generator with built-in pre-and post-processing facilities, *International journal for numerical methods in engineering* 79 (2009) 1309–1331.